An Efficient Power Management Circuit Based on Quasi Maximum Power Point Tracking With Bidirectional Intermittent Adjustment for Vibration Energy Harvesting

Ge Shi, Yinshui Xia, Huakang Xia, Xiudeng Wang, Libo Qian, *Member, IEEE*, Zhidong Chen, Yidie Ye, *Member, IEEE*, and Qing Li

***Abstract*—A power management (PM) circuit based on quasi maximum power point tracking (qMPPT) by maintaining it in maximum power point (MPP) adjacent area is proposed to improve the vibration energy harvesting efficiency. A larger filter capacitor is used to keep the system working in the MPP adjacent area in a long period of time, and the PM circuit can shut down the dc–dc converter for reducing the overall power consumption. When the system deviates from the MPP, a bidirectional buck–boost dc–dc converter turns on to regulate the filter capacitor voltage or extract energy quickly in a short period of time. The experimental results show that the PM circuit can adjust the optimized operating point with the variation of the vibration, the maximum qMPPT efficiency can reach 98.4%, and the maximum end-to-end energy harvesting efficiency can reach 80.6%. The proposed PM circuit can be used in environments permeated with vibration energy to provide energy for the wireless sensor network nodes.**

***Index Terms*—AC–DC power conversion, energy harvesting, maximum power point tracking (MPPT), piezoelectric transducer, power management.**

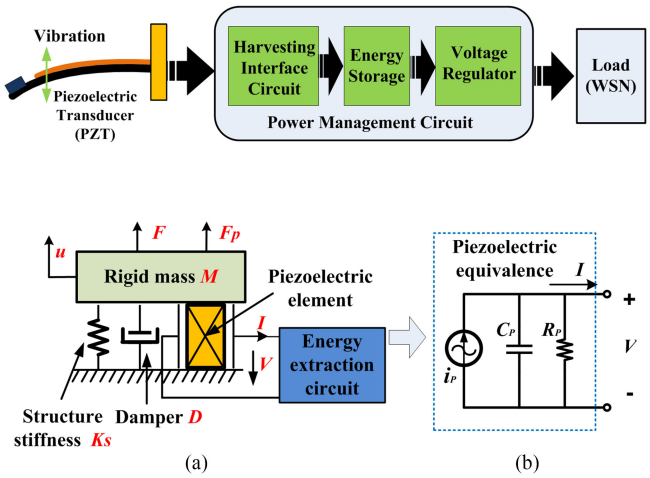

I. Introduction

WIRELESS sensor networks (WSNs) have been used in various applications such as healthcare, home automation, industrial process, and environmental monitoring. However, the battery technique to power nodes of WSNs has become a major bottleneck for battery to be too bulky and heavy with

Manuscript received August 2, 2018; revised October 11, 2018 and November 24, 2018; accepted January 4, 2019. Date of publication January 11, 2019; date of current version June 28, 2019. This work was supported in part by the National Natural Science Foundation of China under Grants U1709218, 61601429, 61801253, and 61771268, in part by the National Key Research and Development Program of China under Grant 2017YFC0804604, in part by Zhejiang Provincial Natural Science Foundation of China under Grants LQ15F010002 and LY17F040002, and in part by the K.C.Wong Magna Fund in Ningbo University. Recommended for publication by Associate Editor M. A. E. Andersen. *(Corresponding author: Yinshui Xia.)*

G. Shi and Q. Li are with the College of Mechanical and Electrical Engineering, China Jiliang University, Hangzhou 310018, China (e-mail:

can be described by a spring mass damping system with only one degree of freedom (equivalent to spring K_S + mass M + damping D + piezoelectric element) [13], where M is the rigid mass, K_S is the structure stiffness, D is the Damper, u is the displacement of rigid mass, F is the external exciting force, F_p is the reaction force of the piezoelectric element acting on the mechanical structure through the inverse piezoelectric effect, V is the voltage of the piezoelectric element output to the energy harvesting circuit, and I is the output current. The governing equations are given by the following [14]:

$$F = M\ddot{u} + D\dot{u} + (K_S + K_{\mathrm{PSC}})u + \alpha V, \tag{1}$$

$$F_p = K_{\mathrm{PSC}}\, u + \alpha\, V, \tag{2}$$

$$I = \alpha\dot{u} - C_p\dot{V} \tag{3}$$

where α and C_p represent the piezoelectric coefficient and the parasitic capacitance, respectively, while K_{PSC} represents the short-circuit stiffness of the piezoelectric element.

The PZT is stimulated by an external force to generate a sinusoidal vibration and its output current reaches the maximum value at its resonance frequency. Its model can be simplified as shown in Fig. 2(b), in which sinusoidal current source i_p, resistor R_p, and parasitic capacitor C_p are connected in parallel [15], [16]. The following analysis assumes that the PZT is based on the simplified circuit model.

The vibrating PZT outputs ac power while nodes of common WSNs need stable dc power supply. Therefore, an ac–dc PM circuit between the PZT and the node of WSNs is required. The classic ac–dc interface circuit is a full-bridge rectifier-based standard energy harvesting (SEH) circuit. However, PZT has a parasitic capacitance C_p and there is always a phase difference between voltage and current, which results in the existence of reactive power. The output characteristic of PZT varies with the environmental condition change, which affects the energy harvesting efficiency. Therefore, the design of PM circuits for harvesting maximal energy from PZT has been investigated intensively in recent years [17]–[20]. The basic principle behind those works is based on impedance matching between PZT and PM circuit. Various kinds of PM circuits have been presented to improve the energy harvesting efficiency, which can be divided into two categories—conjugate matching and resistive matching.

The conjugate matching is implemented with nonlinear treatments. Lefeuvre *et al*. proposed a parallel synchronized switch harvesting on inductor circuit [21]. Badel *et al*. designed a Series Synchronized Switch Harvesting on Inductor (S-SSHI) circuit [14], and furthermore Lefeuvre *et al*. presented a synchronous electric charge extraction (SECE) circuit [22]. Some modified circuits based on these techniques are also available in the public domain, such as double synchronized switch harvesting circuit proposed by Lallart *et al*. [23], enhanced synchronized switch harvesting circuit delivered by Shen *et al*. [24], optimized synchronous electric charge extraction (OSECE) circuit presented by Wu *et al*. [25], self-powered OSECE circuit in [26], self-powered efficient synchronous electric charge extraction circuit proposed by Shi *et al*. [8], and so on. These circuits employ inductors and switches to synchronize the output voltage and current waveforms, and hence equivalently implement the impedance conjugate matching. It is shown that these circuits have potential capability to transfer power higher than the SEH circuit and resistive matching circuit. However, the reaction force introduced by nonlinear treatment such as SSHI and SECE in the process of energy synchronous extraction affects the resonance frequency and vibration amplitude of piezoelectric transducer so that under the same excitation force, the energy harvesting efficiency will be reduced. In this case, the higher the electromechanical coupling coefficient, the lower the energy harvesting efficiency [14].

The resistive matching is based on the assumption that the impedance of a PZT vibrating around the resonant frequency is mostly resistive [15], [27]–[29]. A dc–dc buck converter can be utilized to match the impedance dynamically by modulating the duty ratio [27]. However, a DSP is employed to control the buck converter, which consumes significant power. In order to reduce the power dissipation, the DSP is replaced with discrete components and the step-down converter running at a fixed duty ratio [28], which, however, is unable to implement dynamic impedance matching. Self-powered management circuits delivered by Lefeuvre *et al*. [29] and Kong *et al.* [15] are also incapable of dynamic impedance matching, and hence have low efficiency during vibration condition variation. Kong *et al.* [19] also proposed a system to achieve dynamic resistive matching to improve the harvesting efficiency with the maximum power point tracking (MPPT) executed in a microcontroller unit, in which the filter capacitor voltage and switch ON-time are sampled, and the effective input resistance R_{in} of the converter is computed through software. However, the system just implements the effective input resistance matching without detecting the PZT output voltage. A novel implementation method of maximum power point (MPP) finding based on the $V_{\mathrm{oc,org}}/2$ method is presented by exploiting the capacitor charging voltage across a smoothing capacitor connected in parallel with the energy harvester proposed by Chew and Zhu [30]. It does not need to disconnect the harvesting circuit from the transducer, and the power consumption of the analog control circuit is only 5.16 μW. Due to the existence of the rectifier bridge, the system is unable to harvest energy when the output voltage of PZT is lower than the voltage of the filter capacitor. In a real vibration environment, the vibration amplitude may change frequently. Therefore, it is necessary to study a circuit that can adjust the best working point according to the environment change in time. Recently, some energy harvesting ICs based on MPPT techniques have been developed, such as a 0.35 μm CMOS vibration energy scavenging system with MPPT proposed by Lu *et al.* [31], self-powered piezoelectric energy-harvesting system with 9.09 ms/V tracking time proposed by Shim *et al.* [17]. Those ICs employ the technique with adjusting filter capacitance voltage V_{rect} close to half of open-circuit voltage amplitude for load matching. Hu *et al.* [32] proposed a double-sampling technique, in which the open-circuit voltage is predicted on the basis of point slope formula for MPPT to simplify the measurement circuit. In order to pursue the MPPT tracking speed, these ICs generally use a smaller filter capacitor and adopt a full-time and real-time

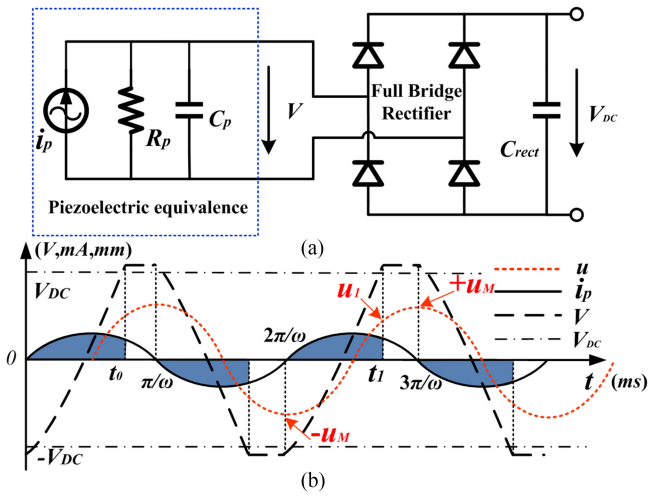

Fig. 3. (a) Common SEH circuit. (b) Its typical waveforms.

adjustment mode, which increases the power consumption of the MPPT and reduces the end-to-end conversion efficiency of the system. In the existing MPPT technology, unidirectional dc–dc is generally used. When the amplitude of the environmental vibration increases rapidly, if a larger filter capacitor is used, it maintains at a lower voltage and cannot be quickly adjusted to the MPP, and the system is in an inefficient situation. If a smaller filter capacitor is used to increase the charging speed, then the dc–dc module is frequently activated and increases the power consumption of the system.

In this paper, a novel filter capacitance voltage regulation PM circuit based on quasi maximum power point tracking (qMPPT) technology is presented for piezoelectric vibration energy harvesting. The principle behind is that high efficiency is maintained in the MPP adjacent area. The MPP is measured with a detection circuit followed after the full-bridge rectifier, and a bidirectional buck–boost dc–dc converter is employed to adjust the input voltage to the MPP adjacent area based on the detection result. A larger filter capacitor is used to keep the system working in the MPP adjacent area in a long period of time, while the PM circuit can shut down the dc–dc converter. When the system deviates from the MPP adjacent area, the bidirectional buck–boost dc–dc converter is turned ON to regulate the filter capacitor voltage or extract energy quickly in a short period of time. This intermittent mode of operation reduces the overall power consumption. The qMPPT control unit added to the rectifier bridge ensures that the system remains at high harvesting efficiency and is independent of the load.

II. Characteristics of the Piezoelectric Energy Harvester

A common SEH interface circuit broadly employed in commercially available energy harvesting chips such as LTC3331, LTC3588-1 from Linear Technology Co. is composed of a full-bridge rectifier and a filter capacitor $C_{\rm rect}$ as shown in Fig. 3(a). The ac voltage output of the PZT is rectified into pulsating dc through the full-bridge rectifier, while $C_{\rm rect}$ is used to reduce the ripple in the dc output.

The process of energy harvesting can be divided into two stages in SEH circuit as shown in Fig. 3(b). Take the positive half-cycle of the equivalent current source i_p for example. In the first stage ($0\sim t_0$), all diodes do not conduct. i_p charges the C_p, in which negative charges are accumulated in the last cycle, so that the output voltage of the PZT rises from the negative to the positive, but there is no output current. In the second stage ($t_0\sim\pi/\omega$), the voltage output of the PZT is twice of diode forward-conduction voltage ($2V_D$) higher than filter capacitor voltage ($V_{\rm DC}$) so that the rectifier turns on. The PZT transfers energy to $C_{\rm rect}$ until the current source is reduced to zero. The typical work waveform is shown in Fig. 3(b), in which t_0 is the turning point between the first stage and the second stage, and during the shadow part of the current waveform i_p the filter capacitor is not charged. The lower the $V_{\rm DC}$, the shorter the time at the first stage, which results in more charges stored in $C_{\rm rect}$ but may not output higher power and vice versa. Specific theoretical analysis is as follows.

Since the charging current is very small, the $V_{\rm DC}$ in half of the vibration cycle deems basically unchanged, and the output power is analyzed by taking the half-cycle ($2\pi/\omega\sim3\pi/\omega$) as an example. As shown in Fig. 3(b), $+u_M$ and $-u_M$ are the peaks of PZT positive displacement and negative displacement of rigid mass, respectively, while u_1 is the corresponding displacement when the output voltage of PZT reaches $V_{\rm DC}$.

Since the output current I is zero at the phase between $-u_M$ and u_1, from (3) and (4) can be obtained

$$\alpha\dot{u} = C_p\dot{V}. \tag{4}$$

According to the analysis of the phase between $-u_M$ and u_1, the following equation can be obtained by integrating the two sides of (4)

$$u_1 - (-u_M) = \frac{C_p \cdot 2V_{\rm DC}}{\alpha}. \tag{5}$$

Similarly, in the case of complete open circuit, there is the relationship of PZT output open-circuit voltage and peak displacement amplitude as in the following equation

$$\alpha u_M = C_p V_{\rm oc,org}. \tag{6}$$

Here, $V_{\rm oc,org}$ is open-circuit voltage amplitude of PZT. If the mechanical vibration frequency of PZT is $f_0 = \omega/2\pi$, then the PZT output power can be expressed as follows:

$$P_{h,\rm SEH} = 2f_0\int_{\frac{2\pi}{\omega}}^{\frac{3\pi}{\omega}} V_{\rm DC} I dt. \tag{7}$$

Since the output current I is zero at the phase between u_M and u_1, the output power is also zero. According to the analysis of the phase between u_1 and $+u_M$, $\dot{V}=0$, from (3), the current during this period is

$$I = \alpha\dot{u}. \tag{8}$$

Substituting (8) into (7) yields the following:

$$P_{h,\rm SEH} = 2f_0\int_{t_1}^{\frac{3\pi}{\omega}} V_{\rm DC}\alpha\dot{u}d_t = 2f_0\alpha V_{\rm DC}(u_M - u_1). \tag{9}$$

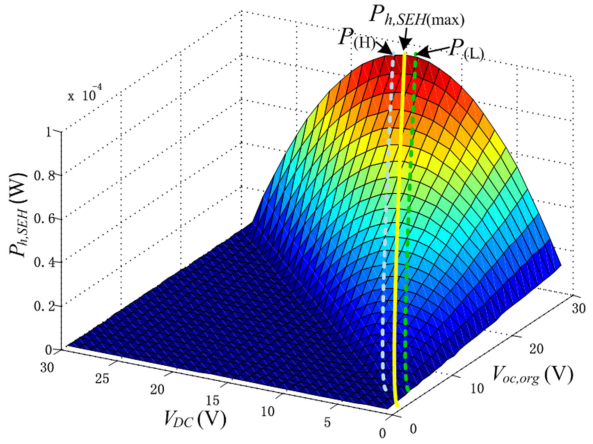

Fig. 4. Effect of $V_{\mathrm{oc,org}}$ and V_{DC} on energy harvesting output power of the SEH circuit ($f_0 = 50$ Hz, $C_p = 220$ nF,$C_{\mathrm{rect}} = 200$ μF).

Then, substituting (5) into (9) yields the following:

$$P_{h,\mathrm{SEH}} = 2f_0\alpha V_{\mathrm{DC}}\left(2u_M - \frac{2C_pV_{\mathrm{DC}}}{\alpha}\right) = 4f_0V_{\mathrm{DC}}(\alpha u_M - C_pV_{\mathrm{DC}}). \quad (10)$$

According to (6) and (10), and taking the diode drop of the rectifier bridge ($2V_D$) into account, the output power of SEH circuit can be obtained

$$P_{h,\mathrm{SEH}} = 4f_0C_pV_{\mathrm{DC}}(V_{\mathrm{oc,org}} - V_{\mathrm{DC}} - 2V_D). \quad (11)$$

It can be seen that the output power of the SEH circuit depends on V_{DC}. $V_{\mathrm{oc,org}}$ depends on the amplitude of the vibration at resonance frequency, which can also affect the output power [33]. According to (11), the derivative of $P_{h,\mathrm{SEH}}$ to V_{DC} is equal to zero when $V_{\mathrm{DC}} = V_{\mathrm{oc,org}}/2 - V_D$. Hence, the SEH circuit can achieve maximum power output

$$P_{h,\mathrm{SEH(max)}} = f_0C_p(V_{\mathrm{oc,org}} - 2V_D)^2. \quad (12)$$

The effect of $V_{\mathrm{oc,org}}$ and V_{DC} on energy harvesting out power of a typical SEH circuit [8] is shown in Fig. 4.

From Fig. 4, it can be seen that in terms of V_{DC}, there is no output power in a wide range since the SEH circuit cannot harvest energy until $V_{\mathrm{oc,org}} > V_{DC} + 2V_D$. There are different MPPs under different $V_{\mathrm{oc,org}}$ conditions. It can harvest maximum $P_{h,\mathrm{SEH(max)}}$ when V_{DC} is near the MPP and $V_{\mathrm{DC}} = V_{\mathrm{oc,org}}/2 - V_D$. High efficiency is maintained near the MPP. In practice, $V_{\mathrm{oc,org}}$ changes from time to time and hence the voltage corresponding to the MPP also varies. Therefore, SEH is hard to guarantee that the system always works at high efficiency.

In this paper, a high-efficiency PM circuit for piezoelectric vibration energy harvesting is proposed by using the qMPPT technology. The principle behind high efficiency is that the energy is extracted in the MPP adjacent area between $P_{(H)}$ and $P_{(L)}$ as shown in Fig. 4. The MPP detection circuit is used to control the bidirectional buck–boost dc–dc circuit to dynamically adjust V_{DC} keeping in the MPP adjacent area. The PM circuit can adjust the working status according to the environment vibration and load variation.

III. Proposed PM Circuit

The proposed PM circuit block diagram for piezoelectric energy harvesting is shown in Fig. 5. It adopts a bidirectional buck–boost dc–dc converter with the constant on-time (COT) modulation for dynamically adjusting V_{DC}. The operation of the PM circuit, low-power design scheme, and the start-up feature are described in this section.

A. PM Circuit Diagram and Its Operation

The full-bridge rectifier converts the ac voltage output from PZT into a pulsating dc waveform V_{rect} (positive voltage of $V_{\mathrm{oc,org}}$) as shown in Fig. 5. Timing control circuit (TCC) controls S_1 and S_2 to switch the PM circuit working modes. When S_1 is turned OFF while S_2 is turned ON, the PZT is disconnected from the C_{rect} of PM circuit, and is basically in the open state since input impedance of MPP detection circuit is very large. The PM circuit switches to the MPP sampling mode. Firstly, the TCC outputs the *Discon* pulse control signal to reset the MPP sampling circuit. Then, MPP samples the V_{rect} and updates the MPP reference level V_{mpp}. When S_1 is turned ON and S_2 is turned OFF, the PM circuit switches to the energy harvesting mode. The PZT is connected to the rectifier bridge and C_{rect} with filtered output voltage V_{DC}. The C_{rect} is connected to a bidirectional dc–dc converter B_1. The output level V_{mpp} of the MPP circuit provides a reference voltage for B_1. The B_1 can adjust the number of pulses and the direction of power transmission so that V_{DC} keeps in the MPP adjacent area.

The V_{DC} of C_{rect} needs to be adjusted to the MPP adjacent area level, and the voltage of the storage capacitor C_{sto}, V_{sto}, may be higher or lower than V_{DC}. Hence, V_{sto} is unstable so that it is hard to provide a stable dc power for the load directly. A unidirectional buck–boost dc–dc converter B_2 is inserted between C_{sto} and load to regulate V_{sto} to a stable V_{out}. The low dropout regulator (LDO) circuit generates a power supply V_{cc} for the TCC, MPP detection circuit, and B_1. V_{DC} is connected via S_3 and D_{10} to C_{sto} for PM circuit self-start-up. In the case of reserve energy shortage, the TTC, MPP detection circuit, and B_1 are in non-working state, S_1, S_3 are turned ON while S_2 is turned OFF. The PZT directly charges C_{rect} and C_{sto} through the full-bridge rectifier as a typical SEH circuit. When the energy accumulated on the C_{sto} is enough to power the B_2 and LDO, the qMPPT circuit can self-start-up. Then, S_3 is turned OFF, and the self-start-up circuit automatically shuts down.

B. Maximum Power Point Detection Circuit

The MPP detection circuit detects the voltage amplitude of the PZT under open-circuit condition. The circuit architecture is shown in Fig. 6. Since V_{rect} is a positive voltage of $V_{\mathrm{oc,org}}$ after the full-bridge rectifier, the operational amplifier of the MPP detection circuit is powered by a single supply V_{cc} for simplifying the circuit. Since the voltage amplitude of the PZT may exceed the operational amplifier operating voltage V_{cc}, let the input voltage of the operational amplifier be 1/20 of the V_{rect}. Hence, the MPP circuit outputs the reference voltage $V_{\mathrm{mpp}} = (V_{\mathrm{oc,org}} - 2V_D)/20$.

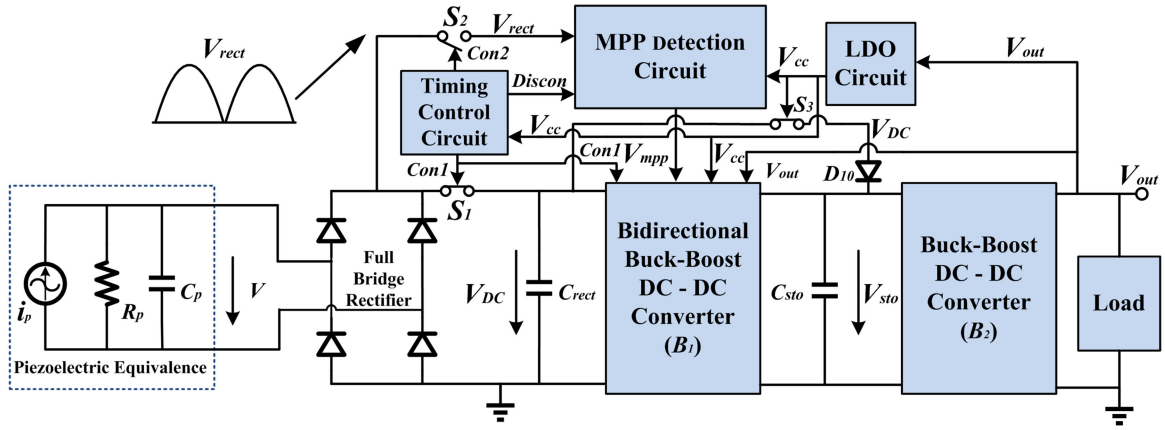

Fig. 5. Architecture of the proposed piezoelectric energy harvesting system.

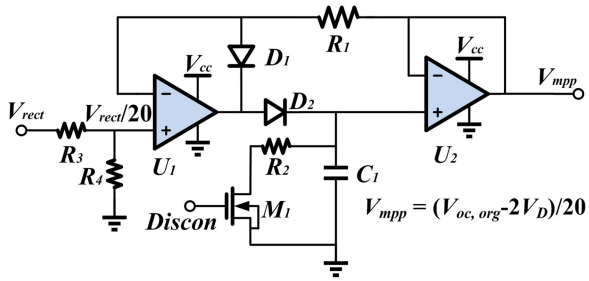

Fig. 6. Proposed maximum power point detection circuit.

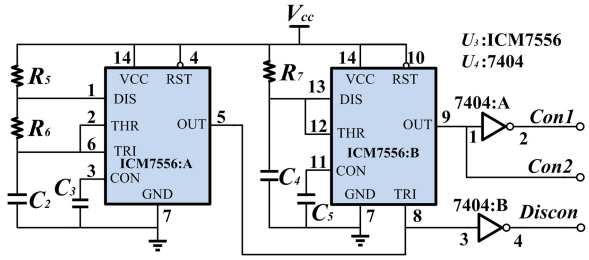

Fig. 7. Proposed timing control circuit.

As shown in Fig. 6, the MPP detection circuit can be divided into several parts

1) resistance divider circuit, input voltage $V_{\rm rect}$ is divided by two resistors in series to obtain $V_{\rm rect}/20$, where $R_3 = 19 \times R_4$, ($R_4 = 50$ KΩ, $R_3 = 950$ KΩ);
2) unidirectional current switches, diodes D_1 and D_2;
3) peak voltage memory, capacitor C_1, which detects and maintains its maximum value by stored charge following $V_{\rm rect}/20$;
4) input and output buffer isolation, that is, operational amplifiers U_1 and U_2, ($R_1 = 1$ KΩ);
5) capacitor discharge reset switch, NMOSFET M_1, when the MPP needs to re-detect, a high level control signal is inputted to the pin Discon to turn ON M_1, so that the capacitor C_1 discharges through $R_2 = 1$ KΩ, then M_1 is turned OFF after the discharge completes, detection circuit begins to re-detect the MPP. The MPP circuit outputs the reference $V_{\rm mpp} = (V_{\rm oc,org} - 2V_D)/20$ for B_1.

Since the input impedance of the operational amplifiers and the resistances of MPP detection circuit are relatively large, the main power consumption of the MPP detection circuit comes from the timing discharge of the detection capacitor, power consumption of $R_3 + R_4$ and operational amplifiers

$$P_{\rm loss,MPP} = \frac{1}{800T_D} C_1 (V_{\rm oc,org} - 2V_D)^2 + \frac{V_{\rm rect}^2}{R_3 + R_4} + 2 \times P_{{\rm loss},OP}. \quad (13)$$

In (13), T_D is the sampling period of the MPP detection circuit. In order to reduce the power consumption of the detection circuit, the sampling frequency needs to be reduced according to the variation of the environmental vibration amplitude.

C. Timing Control Circuit

TCC shown in Fig. 7 controls S_1 and S_2 in Fig. 5 to switch the PM circuit working modes, and the switch M_1 of the MPP detection circuit so that the sampling capacitor C_1 is reset at the sampling initial state. The TCC can adjust the time length of the two working modes by parameter modification according to the application environment vibration amplitude variation.

The TCC uses CMOS general purpose timers, ICM7556, and two NOT gates to realize the control timing signal output. ICM7556 contains two general purpose timer circuits, ICM7556:A and ICM7556:B. As shown in Fig. 7, ICM7556:A, R_5, R_6, and C_2 constitute a multi-vibrator circuit, ($R_5 = 108$ KΩ, $R_6 = 1$ KΩ and $C_2 = 140$ μF). It outputs a square wave signal with several second cycle (T_S) with duty 99%. The square wave signal is inverted by a NOT gate to obtain signal Discon, which resets the MPP detection circuit. ICM7556:B, R_7 and C_4 consist of a mono-stable trigger circuit ($R_7 = 90$ KΩ and $C_5 = 10$ μF). The OUT signal of ICM7556:A outputs a trigger level to the TRI of ICM7556:B. The mono-stable trigger circuit outputs a square wave signal Con2. The cycle is several seconds with duty 10%. Signal Con2 controls S_2 of the $V_{\rm rect}$ sampling circuit path as shown in Fig. 5. Signal Con2 is inverted by a NOT gate to obtain signal Con1, which controls the energy harvesting path switch S_2. The resistance and capacitance parameters of the

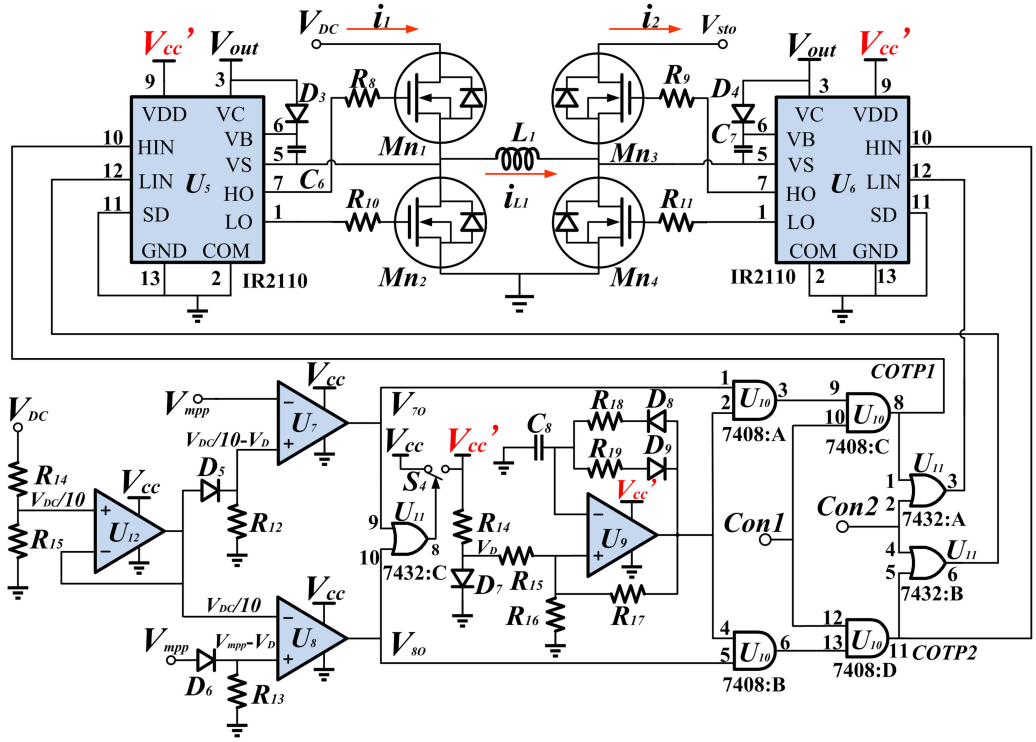

Fig. 8. Proposed bidirectional four-switch buck–boost dc–dc converter circuit.

circuit can be adjusted according to the application environment of the PZT.

The main power consumption of TCC comes from *RC* charging and discharging process. The energy consumed by the multivibrator mainly includes the loss of C_2 charging process by $R_5 + R_6$ and the accumulated energy of C_2 is discharged from $2V_{cc}/3$ to $V_{cc}/3$

$$P_{\text{loss,mul}} = \frac{4{V_{cc}}^2}{9(R_5+R_6)T_D}\int_0^{(R_5+R_6)C_2\ln 2} e^{-\frac{2t}{(R_5+R_6)C_2}}\,dt + \frac{C_2{V_{cc}}^2}{6T_D} \tag{14}$$

$$T_D = \ln 2(R_5+2R_6)C_2. \tag{15}$$

The energy consumed by the mono-stable trigger circuit mainly includes the loss of C_4 charging process by R_7, the accumulated energy of C_4 is discharged from $2V_{cc}/3$ to 0 V and the steady-state power consumption of R_7

$$P_{\text{loss,mon}} = \frac{{V_{cc}}^2}{R_7T_D}\int_0^{R_7C_4\ln 3} e^{-\frac{2t}{R_7C_4}}\,dt + \frac{4C_4{V_{cc}}^2}{9T_D} + \frac{{V_{cc}}^2(T_D - R_7C_4\ln 3)}{R_7T_D} \tag{16}$$

$$P_{\text{loss,TCC}} = P_{\text{loss,mul}} + P_{\text{loss,mon}} + P_{\text{loss},04AB}. \tag{17}$$

The power consumption of TCC includes the power consumption of multi-vibrator oscillator, mono-stable trigger circuit, and digital logic circuit, while the dynamic power consumption of the inverter 7404 ($P_{dyn,04AB}$) can be neglected compared with the other two kinds of power consumption.

D. Bidirectional Buck–Boost DC–DC Converter

The bidirectional buck–boost dc–dc converter B_1 is the most important part of the PM circuit. As shown in Fig. 5, the system can achieve maximum power output when $V_{\text{DC}} = 10 \times V_{\text{mpp}}$, but the voltage of the storage capacitor V_{sto} may be higher or lower than V_{DC}. In this paper, B_1 is used to regulate the V_{DC}. The proposed circuit is shown in Fig. 8.

V_{DC} may be higher than the working voltage of the operational amplifier V_{cc}, and it will be used as a signal for comparison with $V_{\text{mpp}} = (V_{\text{oc,org}} - 2V_D)/20$. Hence, V_{DC} is divided into 1/10 by R_{14} and R_{15} ($R_{14} = 50$ KΩ, $R_{15} = 450$ KΩ). U_{12} implements a voltage follower, and the output voltage $V_{\text{DC}}/10$ is inputted to the following comparator circuits.

Comparator circuits consist of two single power supply rail-to-rail operational amplifiers U_7 and U_8, which respectively constitute two comparator circuits with the same structure, but the inputs of two comparator circuits are different as shown in Fig. 8. Threshold is set when V_{DC} approaches the voltage $10 \times V_{\text{mpp}}$. Only when the voltage difference is greater than the threshold level, the comparator circuits output a control signal to start the bidirectional buck–boost dc–dc converter circuit. Moreover, in order to reduce power consumption, the PM circuit shuts down the modules, which are idle when V_{DC} is within the threshold range. In this paper, two comparator circuits (U_7 and U_8) adopt the diodes (D_5 and D_6) forward voltage $V_D = 0.6$ V as threshold set level as shown in Fig. 8 (D_5 and $R_{12} = 500$ KΩ, D_6 and $R_{13} = 500$ KΩ). When $V_{\text{DC}}/10 - V_D > V_{\text{mpp}}$, the comparator circuit constituted by U_7 outputs high level ($V_{7O} = V_{cc}$), while the output of the comparator constituted by U_8 is 0 V. When $V_{\text{DC}}/10 - V_D < V_{\text{mpp}}$ and $V_{\text{DC}}/10 > V_{\text{mpp}} - V_D$, both

of the comparators constituted by U_7 and U_8 output low level 0 V. When $V_{\rm DC}/10 < V_{\rm mpp} - V_D$, the comparator constituted by U_8 outputs high level ($V_{8O} = V_{cc}$) while that constituted by U_7 outputs low level 0 V. These comparator circuits reflect three operation states between $V_{\rm DC}$ and the target level $10 \times V_{\rm mpp}$. When the voltage difference value is greater than V_D, one of the two comparators outputs a high level, causes the OR-gate 7432:C to output high level and turn ON the switch S_4 to power the rear-end circuits (V'_{cc}), and then COT pulse signal can be generated.

The Schmidt oscillator circuit constituted by U_9 supplies a pulse signal to control the buck–boost converter. The threshold voltages are set using three resistors with the same resistance value ($R_{15} = R_{16} = R_{17} = 500$ KΩ), and the upper and lower thresholds are $V_{\rm TH+} = (V_D + V'_{cc})/3$ and $V_{\rm TH-} = V_D/3$, respectively. The high-level pulsewidth is determined by resistance $R_{18} = 2$ KΩ and capacitance $C_8 = 0.1$ μF through diode D_8 while the low-level pulsewidth is determined by resistance $R_{19} = 8$ KΩ and capacitance C_8 through diode D_9. Two AND-gates (7408:A and 7408:B) are adopted to logically AND the output voltage of U_9 with V_{7O} and V_{8O}, respectively. When $V_{\rm DC}/10 > V_{\rm mpp} + V_D$, 7408:A outputs a COT pulse signal, while 7408:B outputs 0 V. When $V_{\rm DC}/10 < V_{\rm mpp} - V_D$, 7408:B outputs a COT pulse signal, while 7408:A outputs 0 V. When $V_{\rm DC}/10 < V_{\rm mpp} + V_D$ and $V_{\rm DC}/10 > V_{\rm mpp} - V_D$, both 7408:A and 7408:B output 0 V.

When the TCC controls the PM circuit switches to the MPP sampling mode, $V_{\rm mpp}$ is reset, while the buck–boost circuits do not need to work. Control signal Con1 logically ANDs the outputs of 7408:A and 7408:B, respectively. Two AND-gates (7408:C and 7408:D) are adopted to turn OFF the COT pulse signal. When Con1 outputs low level, two AND-gates output 0 V, and then TCC controls the PM circuit switches to the MPP sampling mode. When Con1 outputs high level, two AND-gates output original COT pulse signals (COTP1 or COTP2), and TCC controls the circuit switches to the energy harvesting mode.

Converter B_1 adopts the structure of voltage-controlled traditional discontinuous conduction mode, which uses four NMOSFETS to realize full-bridge control for the input voltage adjustment. As shown in Fig. 8, Mn_1 and Mn_4 are in one group while Mn_2 and Mn_3 are in the other group. The converter controls energy transmitted to $C_{\rm sto}$ from $C_{\rm rect}$ when $V_{\rm DC}/10 > V_{\rm mpp} + V_D$, with Mn_2 and Mn_3 turn OFF during this period. In the first half-period, Mn_1 and Mn_4 are turned ON and $C_{\rm rect}$ transmits energy to inductance L_1. In the latter half-period, Mn_1 and Mn_4 are turned OFF, then inductance L_1 transmits energy to $C_{\rm sto}$ through internal parasitic diodes in Mn_2 and Mn_3. The converter controls energy transmitted to $C_{\rm rect}$ from $C_{\rm sto}$ when $V_{\rm DC}/10 < V_{mpp} - V_D$, with Mn_1 and Mn_4 turn-OFF during this period. In the first half-period, Mn_2 and Mn_3 are turned ON and C_{sto} transmits energy to inductance L_1. In the latter half-period, Mn_2 and Mn_3 are turned OFF and then inductor L_1 transmits energy to $C_{\rm rect}$ through internal parasitic diodes in Mn_1 and Mn_4. The above process ensures that energy harvesting efficiency is achieved in the vicinity of the MPP. Since four switches are all NMOSFETS, so signals COTP1 and COTP2 need a high-voltage side suspension driver IR2110 with bootstrap function to realize the control to four NMOSFETS. In the bootstrap circuits, the bootstrap capacitors C_6 and C_7 need to be pre-charged to make the circuit working normally. C_6 and C_7 are preset to charge during the period of detecting MPP. The control signal Con2 logically ORs COTP1 and COTP2, respectively, by two OR-gates (7432:A and 7432:B) to set two IR2110's LIN pins at high level, so that two VS pins can conduct to the GND in the period of MPP detection. Then, the bootstrap capacitors C_6 and C_7 are pre-charged through D_3 and D_4.

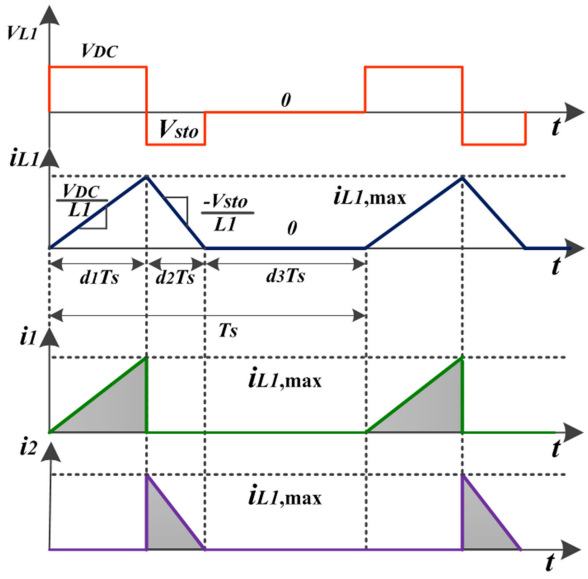

Fig. 9. Simplified waveforms in a forward regulating cycle.

The power dissipation sources of B_1 can be analyzed as follows. It is assumed that the converter runs at a steady state, in which the self-start-up has already been achieved. B_1 does not generate the pulse control signal in the steady state, where $V_{\rm DC}$ has completed the qMPPT. The PM circuit shuts the modules down which do not need to work when $V_{\rm DC}$ is within the threshold range. Therefore, the power consumption of the PM circuit in this case mainly causes from voltage divider resistance, diode and resistance circuits, comparator circuits, and digital logic circuits

$$P_{{\rm loss},B1\,{\rm steady}} = \frac{V_{\rm DC}^2}{10R_{15}} + \frac{(V_{\rm DC}/10)^2 - 2{V_D}^2 + 3(V_{\rm DC}/10)V_D}{R_{12}} + \frac{V_{\rm mpp}^2 - 2V_D^2 + 3V_{\rm mpp}V_D}{R_{13}} + 4P_{{\rm loss},OP} + P_{{\rm loss},32ABC} + P_{{\rm loss},08ABCD}. \quad (18)$$

The energy harvesting efficiency at this state is $P_{\rm har,MPPT}$

$$P_{\rm har,MPPT} = f_0 C_p ({V_{\rm oc,org}}^2 - 4V_{\rm oc,org}V_D). \quad (19)$$

When B_1 runs at the dynamic adjustment state, take the forward regulating process for example. Ideal waveforms in a forward regulating cycle are shown in Fig. 9. For simplicity, the MOSFET, diode, and internal resistance of the inductor are assumed lossless in Fig. 9. The current through inductance L_1 for

one switching cycle is obtained as follows:

$$i_{L1}=\begin{cases}\frac{V_{\rm DC}}{L_1}t, & 0<t\le d_1T_s\\ \frac{V_{\rm DC}d_1T_s}{L_1}-\frac{V_{\rm sto}}{L_1}t, & d_1T_s<t\le(d_1+d_2)T_s\\ 0, & (d_1+d_2)T_s<t\le T_s.\end{cases}\quad(20)$$

In the case of forward regulation, $V_{\rm DC}$ is higher than $10V_{\rm mpp}+V_D$ and the excess energy of the $C_{\rm rect}$ is extracted to the storage capacitor $C_{\rm sto}$ by B_1. The output current of $C_{\rm rect}$ is i_1, while the input current of $C_{\rm sto}$ is i_2. The current directions are shown in Fig. 8. It can be seen that the decrease of $V_{\rm DC}$ is only related to i_1. The waveform of i_1 is shown in Fig. 9. The maximum current of i_1 is equal to the maximum current of i_{L1}

$$i_{1,\max}=i_{L1,\max}=\frac{V_{\rm DC}d_1T_s}{L_1}.\quad(21)$$

Assuming that the voltage change of $V_{\rm DC}$ in a single switching cycle is very small and can be neglected, the energy extracted from $C_{\rm rect}$ in a single switching cycle is as follows:

$$E_{F,\rm single}=\int_0^{d_1T_s}\frac{V_{\rm DC}^2t}{L_1}dt=\frac{(V_{\rm DC}d_1T_s)^2}{2L_1}.\quad(22)$$

The residual energy of $C_{\rm rect}$ after a single switching cycle is as follows:

$$E_{R,\rm single}=\frac{1}{2}C_{\rm rect}V_{\rm DC}^2-\frac{(V_{\rm DC}d_1T_s)^2}{2L_1}=\frac{1}{2}C_{\rm rect}V_{{\rm DC},R-1}^2\quad(23)$$

where $V_{{\rm DC},R-1}$ is the new voltage value of $C_{\rm rect}$ after a switching cycle. The expression of $V_{{\rm DC},R-1}$ can be obtained from (23)

$$V_{{\rm DC},R-1}=V_{\rm DC}\sqrt{1-\frac{(d_1T_s)^2}{L_1C_{\rm rect}}}.\quad(24)$$

According to (24), after N switching cycles, the voltage of $C_{\rm rect}$ drops to the target voltage $10V_{mpp}+V_D$

$$V_{{\rm DC},R-N}=V_{\rm DC}\left[1-\frac{(d_1T_s)^2}{L_1C_{\rm rect}}\right]^{\frac{N}{2}}\le 10V_{\rm mpp}+V_D.\quad(25)$$

Therefore, the required ceiling number of switching cycles is as follows:

$$N=\left\lceil\log_{\sqrt{1-\frac{(d_1T_s)}{L_1C_{\rm rect}}}}\frac{10V_{\rm mpp}+V_D}{V_{\rm DC}}\right\rceil.\quad(26)$$

The value of the filter capacitor in the proposed PM circuit must meet certain conditions. If the filter capacitor $C_{\rm rect}$ is too small, within only one switching cycle, $V_{{\rm DC},R-1}$ may be lower than $10V_{\rm mpp}+V_D$. According to (22) and (24), the value of the filter capacitor must satisfy the following:

$$C_{\rm rect}\gg\frac{V_{\rm DC}(d_1T_s)^2}{4V_D}.\quad(27)$$

The major power loss in N switching cycles is from the power dissipation of three parts—MOSFETS, freewheel diodes of MOSFETs, and the internal parasitic resistance r of L_1.

The loss associated with MOSFETs is mainly the conduction loss and switching loss. The conduction loss is from the channel on-resistance $R_{ds,\rm on}$ and occurs during the switch ON-time. It can be obtained as follows:

$$\begin{aligned}P_{\rm MOSFETs,cond}&=\frac{2}{N+1}\left[\frac{1}{T_S}\int_0^{d_1T_s}\left(\frac{V_{\rm DC}t}{L_1}\right)^2R_{\rm ds,on}dt\right.\\&\quad+\frac{1}{T_S}\int_0^{d_1T_s}\left(\frac{V_{{\rm DC},R-1}t}{L_1}\right)^2R_{\rm ds,on}dt+\cdots\\&\quad\left.+\frac{1}{T_S}\int_0^{d_1T_s}\left(\frac{V_{{\rm DC},R-N}t}{L_1}\right)^2R_{\rm ds,on}dt\right]\\&=\frac{2(V_{\rm DC}d_1)^2T_sR_{\rm ds,on}(1-Z^N)}{3(N+1)L_1(1-Z)}\end{aligned}\quad(28)$$

where parameter Z is introduced to simplify the equation

$$Z=1-\frac{d_1T_s}{L_1C_{\rm rect}}.\quad(29)$$

The switching loss is from the voltage–current overlap during the turn-OFF transition and the output capacitance during the turn-ON transition

$$\begin{aligned}&P_{\rm MOSFETs,OFFloss}\\&=\frac{2}{N+1}\left[\frac{1}{T_S}\int_0^{t_f}\left(\frac{V_{\rm DC}d_1T_s}{L_1}-\frac{V_{\rm DC}d_1T_s}{L_1t_f}t\right)\left(\frac{V_{\rm DC}}{2t_f}t\right)dt\right.\\&\quad+\frac{1}{T_S}\int_0^{t_f}\left(\frac{V_{{\rm DC},R-1}d_1T_s}{L_1}-\frac{V_{{\rm DC},R-1}d_1T_s}{L_1t_f}t\right)\\&\quad\times\left(\frac{V_{{\rm DC},R-1}}{2t_f}t\right)dt+\cdots+\frac{1}{T_S}\int_0^{t_f}\left(\frac{V_{DC,R-N}d_1T_s}{L_1}\right.\\&\quad\left.\left.-\frac{V_{{\rm DC},R-N}d_1T_s}{L_1t_f}t\right)\left(\frac{V_{{\rm DC},R-N}}{2t_f}t\right)dt\right]\\&=\frac{V_{\rm DC}^2d_1t_f(1-Z^N)}{6(N+1)(1-Z)}\end{aligned}\quad(30)$$

$$\begin{aligned}&P_{\rm MOSFETs,ONloss}\\&=\frac{2}{N+1}\left[\frac{1}{2T_S}C_{oss}\left(\frac{V_{\rm DC}}{2}\right)^2+\frac{1}{2T_S}C_{oss}\left(\frac{V_{{\rm DC},R-1}}{2}\right)^2\right.\\&\quad\left.+\cdots+\frac{1}{2T_S}C_{oss}\left(\frac{V_{{\rm DC},R-N}}{2}\right)^2\right]=\frac{C_{oss}V_{\rm DC}^2(1-Z^N)}{4(N+1)T_s(1-Z)}\end{aligned}\quad(31)$$

where t_f is the falling time of the gate input signal, while C_{oss} denotes the output capacitance of the MOSFET.

The forward voltage drop of the diode is expressed as V_F, and the power loss of a diode is $V_F\,i_{L1}$. The current flows through the diode only during the switch OFF-time (d_2T_s). d_2 can be obtained according to (20) and (21)

$$d_2=\frac{V_{\rm DC}d_1}{V_{\rm sto}}.\quad(32)$$

The average conduction loss of the diodes is obtained as follows:

$$\begin{aligned}P_{\mathrm{DIODEs,cond}} &= \frac{2}{N+1}\left[\frac{1}{T_S}\int_0^{d_2T_s} V_F\left(\frac{V_{\mathrm{DC}}d_1T_s}{L_1}-\frac{V_{\mathrm{sto}}}{L_1}t\right)dt\right.\\ &\quad+\frac{1}{T_S}\int_0^{d_2T_s} V_F\left(\frac{V_{\mathrm{DC},R-1}d_1T_s}{L_1}-\frac{V_{\mathrm{sto}}}{L_1}t\right)dt+\cdots\\ &\quad\left.+\frac{1}{T_S}\int_0^{d_2T_s} V_F\left(\frac{V_{\mathrm{DC},R-N}d_1T_s}{L_1}-\frac{V_{\mathrm{sto}}}{L_1}t\right)dt\right]\\ &= \frac{V_{\mathrm{DC}}^2d_1^2T_s(1-Z^N)}{(N+1)L_1V_{\mathrm{sto}}(1-Z)}.\end{aligned} \tag{33}$$

The switching loss of the diodes is only the loss on their junction capacitances during their turn-ON transitions

$$P_{\mathrm{DIODEs,ONloss}} = \frac{1}{4T_S}C_jV_{\mathrm{sto}}^2 \tag{34}$$

where C_{j} is the diode capacitance.

The loss associated with the inductance is mainly due to the parasitic resistance r of the copper wires. It can be obtained as follows:

$$P_{L1,r\mathrm{loss}} = \frac{1}{N+1}\left\{\begin{array}{l}\frac{1}{T_S}\left[\int_0^{d_1T_s}\left(\frac{V_{\mathrm{DC}}t}{L_1}\right)^2 r dt\right.\\ \quad\left.+\int_0^{d_2T_s}\left(\frac{V_{\mathrm{DC}}d_1T_s}{L_1}-\frac{V_{sto}}{L_1}t\right)^2 r dt\right]\\ +\frac{1}{T_S}\left[\int_0^{d_1T_s}\left(\frac{V_{\mathrm{DC},R-1}t}{L_1}\right)^2 r dt\right.\\ \quad\left.+\int_0^{d_2T_s}\left(\frac{V_{\mathrm{DC},R-1}d_1T_s}{L_1}-\frac{V_{sto}}{L_1}t\right)^2 r dt\right]\\ +\cdots+\frac{1}{T_S}\left[\int_0^{d_1T_s}\left(\frac{V_{\mathrm{DC},R-N}t}{L_1}\right)^2 r dt\right.\\ \quad\left.+\int_0^{d_2T_s}\left(\frac{V_{\mathrm{DC},R-N}d_1T_s}{L_1}-\frac{V_{sto}}{L_1}t\right)^2 r dt\right]\end{array}\right\}. \tag{35}$$

The bootstrap driver IR2110 and the oscillator circuit consume the amount of power during this process, and the power dissipation required for steady-state processes also persists in the forward regulation. The power loss in the forward regulating process can be obtained

$$\begin{aligned}P_{\mathrm{loss,forward}} &= P_{\mathrm{MOSFETs,cond}}+P_{\mathrm{MOSFETs,OFFloss}}\\ &\quad+P_{\mathrm{MOSFETs,ONloss}}+P_{\mathrm{DIODEs,cond}}\\ &\quad+P_{\mathrm{DIODEs,ONloss}}+P_{L1,r\mathrm{loss}}+P_{\mathrm{loss},B1\mathrm{steady}}\\ &\quad+P_{\mathrm{OSC,loss}}+P_{IR2110,\mathrm{loss}}.\end{aligned} \tag{36}$$

The energy transferred to C_{sto} during the forward regulating process can be expressed as follows:

$$\begin{aligned}E_{\mathrm{har,forward}} &= \frac{1}{2}C_{\mathrm{rect}}V_{\mathrm{DC}}^2-\frac{1}{2}C_{\mathrm{rect}}(V_{\mathrm{DC}}-10V_{\mathrm{mpp}}-V_D)^2\\ &\quad-(N+1)T_sP_{\mathrm{loss,forward}}.\end{aligned} \tag{37}$$

When the MPP detection circuit detects that the PZT output voltage increases and V_{DC} is at a relatively low voltage, it goes into reverse regulating process and reverses the energy from C_{sto} to C_{rect}, which is similar to the previous forward regulating process analysis and is not discussed in detail here. It is noteworthy that due to different adjustment of the object (current direction, voltages V_{DC} and V_{sto}, element, etc.), the loss is a floating one and varies from case to case

$$\begin{aligned}P_{\mathrm{loss,reverse}} &= P'_{\mathrm{MOSFETs,cond}}+P'_{\mathrm{MOSFETs,OFFloss}}\\ &\quad+P'_{\mathrm{MOSFETs,ONloss}}+P'_{\mathrm{DIODEs,cond}}\\ &\quad+P'_{\mathrm{DIODEs,ONloss}}+P'_{L1,r\mathrm{loss}}\\ &\quad+P_{\mathrm{loss},B1\mathrm{steady}}+P_{\mathrm{OSC,loss}}+P_{IR2110,\mathrm{loss}}.\end{aligned} \tag{38}$$

E. Buck–Boost DC–DC Converter and LDO

Since V_{sto} is unstable, it cannot provide a steady dc power directly. Therefore, B_2 is used to regulate output voltage to output stable V_{out} at the end of the C_{sto}. Output voltage V_{out} provides a stable power for LDO and cascades B_1. LDO outputs V_{cc} to provide a stable power for TCC and MPP detection circuit.

The energy of these two parts is mainly determined by the circuit itself and the load condition. The detailed analysis is not carried out here.

The qMPPT harvesting efficiency η_{MPPT} is defined as the ratio of the harvested maximum power $P_{\max}$ on the C_{rect} to the power P_{in} flowing into the harvesting system

$$\eta_{\mathrm{MPPT}} = \frac{P_{\max}}{P_{\mathrm{in}}}\times 100\%. \tag{39}$$

The conversion harvesting efficiency $\eta_{\mathrm{conversion}}$ is defined as the ratio of the harvested power P on the different tested point to the power P_{in} flowing into the harvesting system

$$\eta_{\mathrm{conversion}} = \frac{P}{P_{\mathrm{in}}}\times 100\%. \tag{40}$$

IV. Experimental Results

A. Prototyping and Experimental Setup

To verify the feasibility and measure the performance of the proposed PM circuit for piezoelectric energy harvesting, a prototype system is built and the experiment is carried out. The experimental setup is shown in Fig. 10, which is built up with a piezoelectric cantilever and the proposed PM circuit. The main mechanical structure is a copper cantilever in which one terminal is fixed by mounting bracket on the shaker, while the other one is free. A piezoelectric patch of 80 mm × 40 mm × 0.3 mm is bonded on the cantilever. A set of screws and nuts are attached at the free terminal of the cantilever, acting as a rigid mass to lower the vibration frequency and increase the displacement of the free terminal. Piezoelectric cantilever is stimulated by a shaker.

A shaker (ZJ-2A, Shanghai Zhurui Co.) is excited at the natural frequency of the cantilever and driven by a sine wave from a function generator (DG3121A, RIGOL Co.), that is amplified

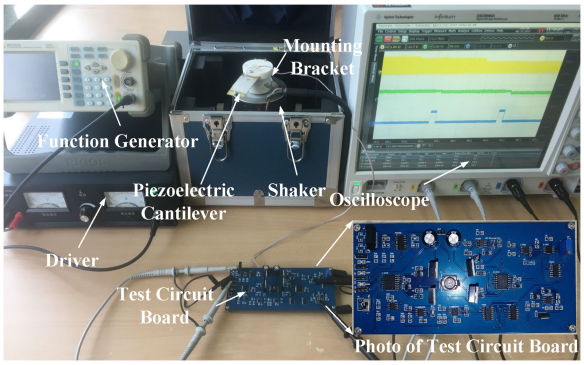

Fig. 10. Experimental setup used for measurements, based on the test board and a piezoelectric cantilever stimulated by a shaker.

TABLE I
MODELS OR VALUES OF COMPONENT USED IN EXPERIMENTS

Component	Models or values
Parasitic Capacitance of PZT(C_p)	840 (nF)
Internal Resistance of PZT (R_p)	2 (MΩ)
Rectifier	BAS3007
NMOSFETs(Mn_1~Mn_4)	IRF3205
Diodes(D_1~D_{10})	MBRA120
Analog Switches(S_1~S_4)	MAX393
Inductor(L)	1.5 (mH)
Internal Resistance of L(r)	1.4 Ω
Rectified Filter Capacitor (C_{rect})	1500 (μF)
Energy-storage Capacitor(C_{sto})	0.06 (F)
Operational Amplifier (U_1, U_2, U_7, U_8, U_9, U_{12})	OPA2333
DC-DC Converter (B_2)	LTC3112
LDO	SPX5205M5-5.0

by a power amplifier (GF-20W, Shanghai Zhurui Co.). An oscilloscope (DSO9064A, Agilent Co.) is employed to observe the voltage waveform in the energy harvesting process. A PCB board is designed to test the performance of the proposed PM circuit for piezoelectric energy harvesting. The values of the used external components are listed in Table I. The value of $C_{\rm sto}$ may affect the performance of the system. If $C_{\rm sto}$ is too large, the self-starting process time of the system is too long. Otherwise, the energy storage may be insufficient and load may not work normally. Hence, the value of $C_{\rm sto}$ needs to be chosen properly according to the vibration environment and load conditions.

B. MPP Detection and qMPPT Process Test

The MPP detection circuit detects the voltage amplitude of the PZT under open-circuit condition. The test waveforms of MPP detection circuit are shown in Fig. 11. In the energy harvesting mode, S_2 is turned OFF, and there is no signal input on $V_{\rm rect}$ side of MPP detection circuit. Hence, the voltage waveform of $V_{\rm rect}$ keeps at low level, and $V_{\rm mpp}$ is unchanged. In the MPP sampling mode, S_2 is turned ON, the voltage waveform of $V_{\rm rect}$ is the vibration waveform after PZT rectification (20 Hz for better viewing of the waveform). $V_{\rm mpp}$ follows the vibration amplitude voltage change when Discon changes to high level

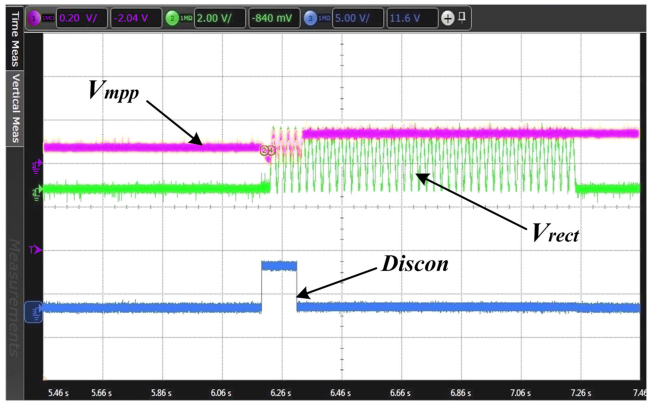

Fig. 11. Experimental waveforms of MPP detection circuit.

and discharges the sampling capacitor, and $V_{\rm mpp}$ outputs the vibration peak voltage when Discon changes to low level.

The experimental waveforms of qMPPT process are shown in Fig. 12 when the amplitude of vibration is changed. The voltage waveform of piezoelectric vibration sensor is displayed in channel 1 of oscilloscope. The output amplitude of the piezoelectric vibration sensor is set to equal to the output value of PZT. The shaker varies the amplitude of the vibration by adjusting the function generator. As shown in Fig. 12, the vibration amplitude first is slowly increased, and then quickly reduced. The waveform of Con2 is displayed through channel 3 and $V_{\rm DC}$ is through channel 2. The piezoelectric energy harvesting PM circuit is in the MPP sampling process when Con2 is at high level (such as: t_0~t_1, t_3~t_4, etc.). $V_{\rm DC}$ remains unchanged as shown in channel 2 during this process. $V_{\rm DC}$ changes under two cases after the MPP sampling process. 1)$V_{\rm DC}$ is not adjusted when the change of vibration amplitude is less than the threshold such as after t_4, t_5, etc. 2)$V_{\rm DC}$ is adjusted when the change of vibration amplitude is larger than the threshold after the MPP sampling process such as in t_1~t_2, t_6~t_7, etc. During the period t_1~t_2, $V_{\rm DC}$ rises and B_1 transfers energy from $C_{\rm sto}$ to $C_{\rm rect}$. The qMPPT process is completed after $V_{\rm DC}$ is adjusted, and the piezoelectric energy harvesting PM circuit enters the energy harvesting process such as in t_2~t_3. During the period t_6~t_7, $V_{\rm DC}$ is quickly reduced and B_1 transfers energy from $C_{\rm rect}$ to $C_{\rm sto}$. As shown in Fig. 12, the circuit can realize the qMPPT very well under the current parameters. In the actual work process, the MPP sampling frequency should be adjusted to meet the changing requirements of the actual vibration environment.

C. Start-Up and qMPPT Effect

The piezoelectric energy harvesting PM circuit can be self-started-up without reserve power. The PZT directly charges $C_{\rm rect}$ and $C_{\rm sto}$ through the full-bridge rectifier as a typical SEH circuit. When the LDO outputs V_{cc} and S_3 is turned OFF, the maximum efficiency tracking PM circuit can be self-started-up. Since B_2 uses LTC3112 and its input minimum operating voltage is 2.7 V, when the piezoelectric vibration output voltage amplitude is higher than 3.54 V, the circuit can charge the capacitor through the rectifier and diode to self-start-up maximum

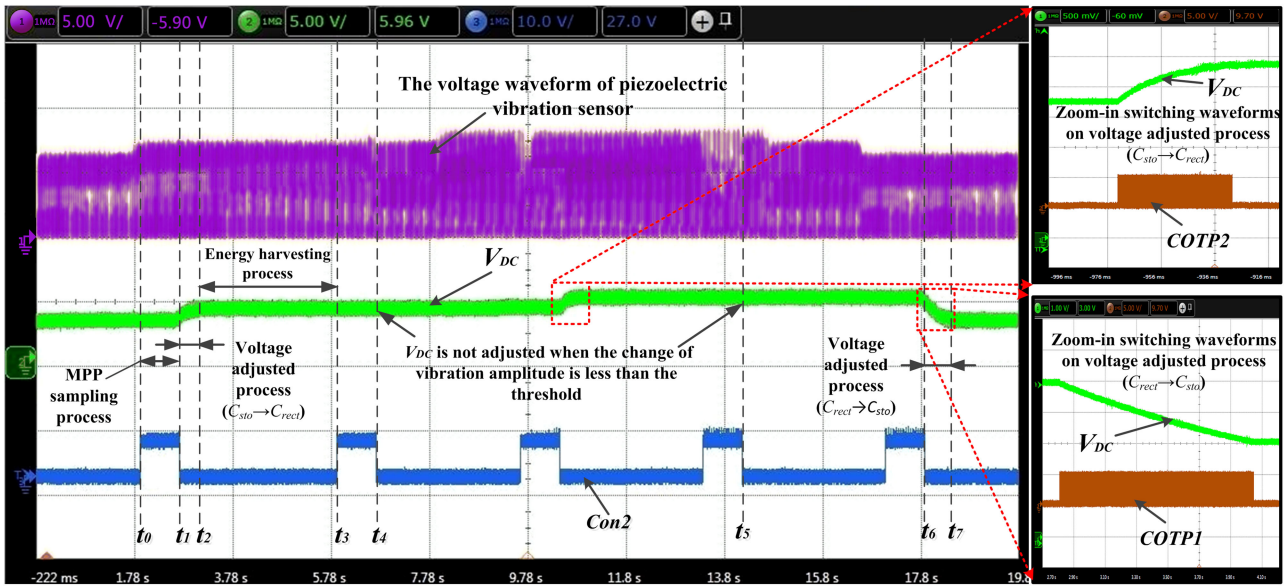

Fig. 12. Experimental waveforms of qMPPT process when the amplitude of vibration is changed.

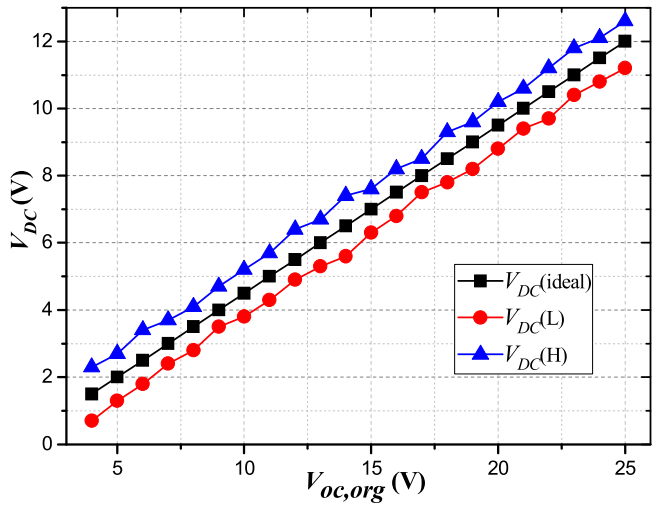

Fig. 13. Tested voltage V_{DC} of C_{rect} under different $V_{\mathrm{oc,org}}$.

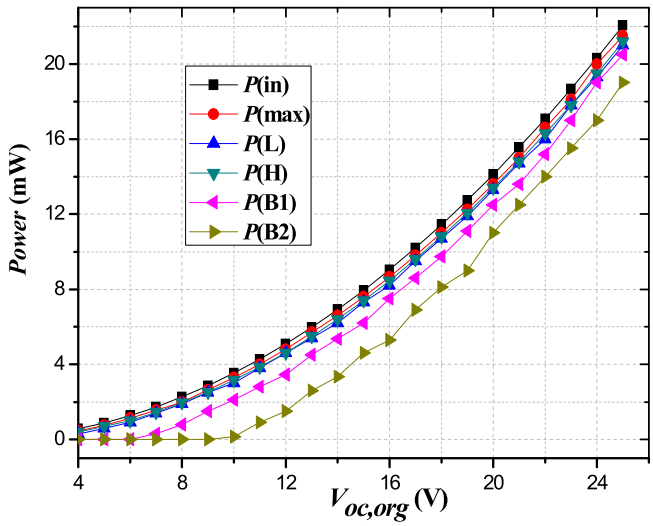

Fig. 14. Tested power under different $V_{\mathrm{oc,org}}$.

efficiency tracking PM circuit. In the event of insufficient energy of capacitor C_{sto} ($V_{\mathrm{sto}} < 2.7$ V), B_2 ceases to operate until the vibration energy reaches the threshold ($V_{\mathrm{oc,org}} > 3.54$ V) and enough energy is saved ($V_{\mathrm{sto}} > 2.7$ V).

The qMPPT process effect is tested under sufficient conditions of system energy storage. Tested voltage V_{DC} of C_{rect} under different $V_{\mathrm{oc,org}}$ is shown in Fig. 13. Two test curves, V_{DC}(H) and V_{DC}(L), are obtained respectively with increasing or decreasing amplitude of the vibration voltage output ($V_{\mathrm{oc,org}} > 4$ V). As shown in the Fig. 13, the range of two test curves is always around the ideal maximum power tracking point (V_{DC}(ideal)±0.7 V), and circuit can well track the MPP of PZT.

D. Output Power and Efficiency

The input power P(in) and different power outputs are tested for the proposed PM circuit under different $V_{\mathrm{oc,org}}$. As shown in Fig. 14, the harvested power on the rectifier capacitor C_{rect} is shown in P(H), P(L), and P(max). P(H) and P(L) are the power outputs when the amplitude increases and decreases, respectively. P(max) is the maximum power output in the adjusting process. The harvested power on the energy storage capacitor C_{sto} behind B_1 is shown in P(B1). As shown in P(B1), when the vibration amplitude $V_{\mathrm{oc,org}} < 5.9$ V, P(in) is less than the power consumption of B_1. B_1 cannot normally output power in the absence of sufficient energy storage. The harvested power on the load behind the convertor B_2 is shown in P(B2). When the vibration amplitude $V_{\mathrm{oc,org}} > 9.8$ V, the input power of the system is higher than the PM circuit power consumption. The system can work normally and output power to the load.

According to the output power and input power, the harvesting efficiency curves of each stage are shown in Fig. 15. The harvesting efficiency increases with the maximum vibration amplitude. From curve E(H), when the vibration amplitude $V_{\mathrm{oc,org}}$

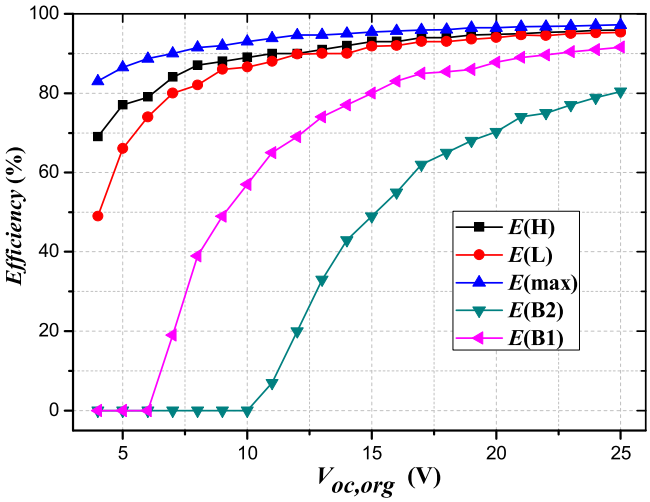

Fig. 15. Tested conversion and system efficiency under different $V_{\mathrm{oc,org}}$.

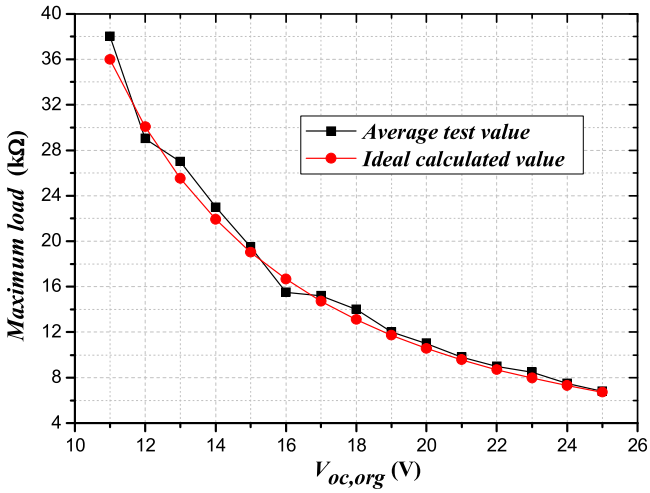

Fig. 16. Tested maximum load under different $V_{\mathrm{oc,org}}$.

is 25 V, the η_{MPPT} of the PM circuit can reach 98.4%. From curve E(B2), the system harvesting efficiency is 0 for the harvested energy is less than PM circuit consumption when the vibration amplitude $V_{\mathrm{oc,org}} < 9.8$˜V. When the vibration amplitude $V_{\mathrm{oc,org}}$ is 25 V, the maximum end-to-end efficiency of the PM circuit can reach 80.6%.

E. Load Testing and Breakdown of the Losses

The load ability of the proposed PM circuit is tested under different vibration amplitude conditions, as shown in Fig. 16. The larger the vibration voltage amplitude, the smaller the resistance value and the higher the output power.

The power loss of the components is the critical factor for the system efficiency. Fig. 17 shows the loss breakdown including basic and floating loss under normal operating condition. B_1 and B_2 are the major sources and account for 34% and 27% of the total power loss, respectively. The power loss of the LDO is mainly the voltage drop loss. The maximum power consumption of the circuit is 3.69 mW.

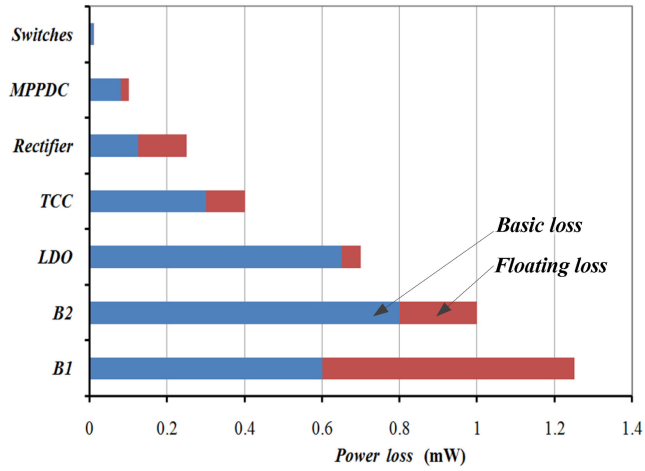

Fig. 17. Breakdown of the power loss.

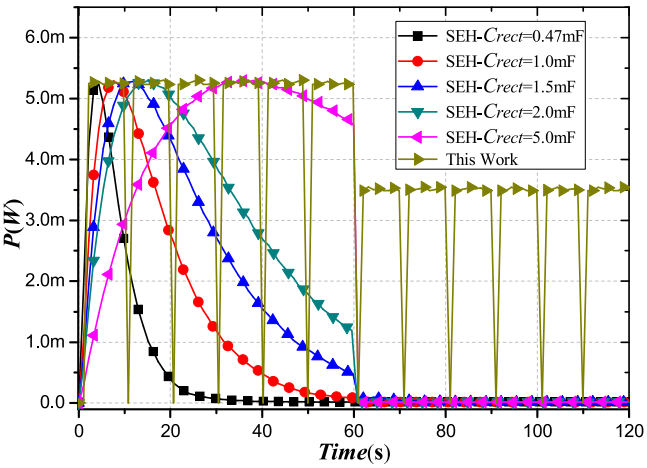

Fig. 18. Power comparison between the proposed system and the SEH with different C_{rect} when the vibration amplitude changes.

F. Comparison With Other Systems

To compare the energy harvesting power with and without the proposed PM circuit, SEH circuits with different values of C_{rect} (0.47,1.0, 1.5, 2.0, and 5.0 mF) are tested. In the proposed PM circuit, C_{rect} is 1.5 mF. Let the initial voltage of all capacitors be 0 V. The experiment simulates a common environmental vibration amplitude change process. In the first minute, the PZT's output voltage $V_{\mathrm{oc,org}}$ is 15 V, but it is reduced to 10 V in the second minute. The instantaneous power is calculated by measuring the change in C_{rect} voltage over time. The experimental results are shown in Fig. 18. In the first minute, the charging speed of the smaller capacitor (such as 0.47 mF) is faster. But as the voltage of the smaller capacitor approaches the $V_{\mathrm{oc,org}}$, the harvested power of the smaller capacitor begins to decrease. And it does not harvest energy until 30 s. The power curve shapes of the larger capacitors (such as 1.5, 2.0,F and 5.0 mF) are basically similar. But the charging speeds are slower than those of the smaller capacitors, and the starting power is lower than that of smaller capacitors too. The charging process of larger capacitors is continued in the first minute. But as the voltage of the C_{rect} increases, the harvesting power is getting lower and lower.

TABLE II
COMPARISON OF PE ENERGY HARVESTING SYSTEMS

Publication	TVLSI2011 [31]	TPE2012 [19]	JSSC2015 [17]	ASSCC2016 [32]	This Work
Advantage of technology	2 cycles sampling	Dynamical resistor matching	MPPT fast tracking	Voltage prediction	Bidirectional converter Intermittent mode
Input voltage	~6.5V	3~25V	1~7V	6.6V	3.54~25V
Frequency	200Hz	47Hz	N/A	200Hz	50Hz
Converter type	Buck	Buck-boost	Buck-boost	Buck-boost	Buck-boost
MPPT algorithm	Fractional $V_{oc,org}$	Resistor matching	Fractional $V_{oc,org}$	Prediction $V_{oc,org}$	Fractional $V_{oc,org}$
Maximum MPPT efficiency	98.2%	94%	99%	98.7%	98.4%
Maximum end to end conversion efficiency	N/A	76%	80%	73%	80.6%

Compared with these circuits, the harvesting power of the proposed circuit is rapidly increased even if its initial voltage is 0 V. This is that the proposed circuit can start the reverse adjustment function of the bidirectional buck–boost dc–dc converter. And the higher harvesting power is maintained in the first minute. In the second minute, due to the rapid decrease in the amplitude of the vibration voltage, when the rectifier bridge is turned off, the instantaneous power of the SEH circuit falls down suddenly. Based on the automatic detection of MPP detection circuit, the proposed PM circuit starts the forward adjustment function of the bidirectional buck–boost dc–dc converter, and re-tracks the instantaneous power to the new MPP. As shown in Fig. 18, the instantaneous power of the proposed circuit is maintained at a high level throughout the process except sampling and adjustment stages.

Table II lists the comparison of the proposed PM circuit-based energy harvesting system and other reported PE energy harvesting systems. The maximum power consumption of the proposed PM circuit system is about 3.69 mW. The maximum harvested power is about 19.5 mW, the maximum qMPPT efficiency can reach 98.4% while the maximum end-to-end energy harvesting efficiency can reach 80.6% when the vibration voltage amplitude $V_{\mathrm{oc,org}}$ is 25 V. In [19], the resistor matching is realized by the real-time control of the output current through C_{rect}. The system uses an MCU to realize real-time voltage sampling and switching control, hence the overall conversion efficiency is only 76%. In [17], [31], and [32], different methods are used to optimize the sampling speed of $V_{\mathrm{oc,org}}$. However, all of these systems use unidirectional dc–dc converters to realize fractional $V_{\mathrm{oc,org}}$. When the amplitude of the environmental vibration increases rapidly, the adjustment of the V_{DC} can only be completed by the charging of PZT to the filter capacitor slowly. If the system is required to quickly adjust to new MPP, then only a smaller capacitor can be used, which means that the switching loss of the dc–dc circuit will be increased. Therefore, the end-to-end conversion efficiency of those systems are not very high. In this work, some discrete components are high in energy consumption, and the end-to-end conversion efficiency is affected. If the scheme is designed as a single chip, the end-to-end conversion efficiency will be even improved. Hence, the qMPPT-based proposed PM circuit with bidirectional buck–boost dc–dc converter and intermittent mode of operation are advantageous to improve the end-to-end energy harvesting efficiency.

V. CONCLUSION

A novel qMPPT PM circuit based on filter capacitance voltage regulation for piezoelectric vibration energy harvesting is presented in this paper. It uses the principle that high efficiency is maintained near the MPP adjacent area. A larger filter capacitor is used to keep the system working in MPP adjacent area in a long period of time, and the PM circuit can shut down the dc–dc converter. When the system deviates from the MPP adjacent area, a bidirectional buck–boost dc–dc converter is turned ON to regulate the filter capacitor voltage or extract energy quickly in a short period of time. This intermittent mode of operation reduces the overall power consumption. The experimental results show that the harvesting circuit can accurately adjust the optimal operating point with the variation of the vibration, the maximum qMPPT efficiency can reach 98.4% while the maximum end-to-end energy harvesting efficiency can reach 80.6% when the vibration voltage amplitude $V_{\mathrm{oc,org}}$ is 25 V. Future works include adaptive control of sampling frequency and development of an efficient circuit in a monolithic IC. Finally, the proposed PM circuit can be used in environments filled with vibration energy to provide energy for the wireless sensor network nodes of environmental monitoring.

REFERENCES

[1] S. Bandyopadhyay and A. P. Chandrakasan, "Platform architecture for solar, thermal, and vibration energy combining with MPPT and single inductor," *IEEE J. Solid-State Circuits*, vol. 47, no. 9, pp. 2199–2215, Sep. 2012.

[2] D. Porcarelli, D. Spenza, D. Brunelli, A. Cammarano, C. Petrioli, and L. Benini, "Adaptive rectifier driven by power intake predictors for wind energy harvesting sensor networks," *IEEE J. Emerg. Sel. Topics Power Electron.*, vol. 3, no. 2, pp. 471–482, Jun. 2015.

[3] T. Ogawa, T. Ueno, T. Miyazaki, and T. Itakura, "20 mV input, 4.2 V output boost converter with methodology of maximum output power for thermoelectric energy harvesting," in *Proc. IEEE Appl. Power Electron. Conf. Expo.*, 2016, pp. 1907–1910.

[4] S. Hemour et al., "Towards low-power high-efficiency RF and microwave energy harvesting," *IEEE Trans. Microw. Theory Techn.*, vol. 62, no. 4, pp. 965–976, Apr. 2014.

[5] P. D. Gleonec, J. Ardouin, M. Gautier, and O. Berder, "Architecture exploration of multi-source energy harvester for IoT nodes," in *Proc. IEEE Online Conf. Green Commun.*, 2016, pp. 27–32.

[6] A. Agbossou, Q. Zhang, G. Sebald, and D. Guyomar, "Solar micro-energy harvesting based on thermoelectric and latent heat effects. Part I: Theoretical analysis," *Sens. Actuators A, Phys.*, vol. 163, no. 1, pp. 277–283, Sep. 2010.

[7] L. A. J. Friedrich, J. J. H. Paulides, and E. A. Lomonova, "Modeling and optimization of a tubular generator for vibration energy harvesting application," *IEEE Trans. Magn.*, vol. 53, no. 11, Nov. 2017, Art. no. 8209804.

[8] G. Shi, Y. Xia, Y. Ye, L. Qian, and Q. Li, "An efficient self-powered synchronous electric charge extraction interface circuit for piezoelectric energy harvesting systems," *J. Intell. Mater. Syst. Struct.*, vol. 27, no. 16, pp. 2160–2178, Jan. 2016.

[9] J. Sankman and M. Dongsheng, "A 12-μW to 1.1-mW AIM piezoelectric energy harvester for time-varying vibrations with 450-nA I Q," *IEEE Trans. Power Electron.*, vol. 30, no. 2, pp. 632–643, Feb. 2015.

[10] A. L. F. Stein and H. F. Hofmann, "Autonomous wideband piezoelectric energy harvesting utilizing a resonant inverter," *IEEE Trans. Power Electron.*, vol. 32, no. 8, pp. 6178–6187, Aug. 2017.
[11] J.-Q. Liu et al., "A MEMS-based piezoelectric power generator array for vibration energy harvesting," *Microelectron. J.*, vol. 39, no. 5, pp. 802–806, May 2008.
[12] E. E. Aktakka and K. Najafi, "A micro inertial energy harvesting platform with self-supplied power management circuit for autonomous wireless sensor nodes," *IEEE J. Solid-State Circuits*, vol. 49, no. 9, pp. 2017–2029, Jun. 2014.
[13] D. Guyomar, A. Badel, E. Lefeuvre, and C. Richard, "Toward energy harvesting using active materials and conversion improvement by nonlinear processing," *IEEE Trans. Ultrason., Ferroelect., Freq. Control*, vol. 52, no. 4, pp. 584–595, Apr. 2005.
[14] E. Lefeuvre, A. Badel, C. Richard, L. Petit, and D. Guyomar, "A comparison between several vibration-powered piezoelectric generators for standalone systems," *Sens. Actuators A, Phys.*, vol. 126, no. 2, pp. 405–416, Feb. 2006.
[15] N. Kong, D. S. Ha, A. Erturk, and D. J. Inman, "Resistive impedance matching circuit for piezoelectric energy harvesting," *J. Intell. Mater. Syst. Struct.*, vol. 21, no. 13, pp. 1293–1302, Jan. 2010.
[16] Y. K. Ramadass and A. P. Chandrakasan, "An efficient piezoelectric energy harvesting interface circuit using a bias-flip rectifier and shared inductor," *IEEE J. Solid-State Circuits*, vol. 45, no. 1, pp. 189–204, Jan. 2010.
[17] M. Shim, J. Kim, J. Jeong, S. Park, and C. Kim, "Self-powered 30μW to 10 mW piezoelectric energy harvesting system with 9.09 ms/V maximum power point tracking time," *IEEE J. Solid-State Circuits*, vol. 50, no. 10, pp. 2367–2379, Oct. 2015.
[18] X. D. Do, S. K. Han, and S. G. Lee, "Optimization of piezoelectric energy harvesting systems by using a MPPT method," in *Proc. IEEE 5th Int. Conf. Commun. Electron.*, 2014, pp. 309–312.
[19] N. Kong and D. S. Ha, "Low-power design of a self-powered piezoelectric energy harvesting system with maximum power point tracking," *IEEE Trans. Power Electron.*, vol. 27, no. 5, pp. 2298–2308, May 2012.
[20] S. Fan, R. Wei, L. Zhao, X. Yang, L. Geng, and P. X. L. Feng, "An ultralow quiescent current power management system with maximum power point tracking (MPPT) for batteryless wireless sensor applications," *IEEE Trans. Power Electron.*, vol. 33, no. 5, pp. 7326–7337, Sep. 2018.
[21] E. Lefeuvre, A. Badel, C. Richard, and D. Guyomar, "High performance piezoelectric vibration energy reclamation," *Proc. SPIE*, vol. 5390, pp. 379–387, 2004.
[22] E. Lefeuvre, A. Badel, C. Richard, and D. Guyomar, "Piezoelectric energy harvesting device optimization by synchronous electric charge extraction," *J. Intell. Mater. Syst. Struct.*, vol. 16, no. 10, pp. 865–876, Oct. 2005.
[23] M. Lallart, L. Garbuio, L. Petit, C. Richard, and D. Guyomar, "Double synchronized switch harvesting (DSSH): A new energy harvesting scheme for efficient energy extraction," *IEEE Trans. Ultrason. Ferroelect. Freq. Control*, vol. 55, no. 10, pp. 2119–2130, Oct. 2008.
[24] H. Shen, J. H. Qiu, H. L. Ji, K. J. Zhu, and M. Balsi, "Enhanced synchronized switch harvesting: A new energy harvesting scheme for efficient energy extraction," *Smart Mater. Struct.*, vol. 19, no. 11, Nov. 2010, Art. no. 115017.
[25] Y. P. Wu, A. Badel, F. Formosa, W. Q. Liu, and A. E. Agbossou, "Piezoelectric vibration energy harvesting by optimized synchronous electric charge extraction," *J. Intell. Mater. Syst. Struct.*, vol. 24, no. 12, pp. 1445–1458, Aug. 2013.
[26] Y. P. Wu, A. Badel, F. Formosa, W. Q. Liu, and A. Agbossou, "Self-powered optimized synchronous electric charge extraction circuit for piezoelectric energy harvesting," *J. Intell. Mater. Syst. Struct.*, vol. 25, no. 17, pp. 2165–2176, Nov. 2014.
[27] G. K. Ottman, H. F. Hofmann, A. C. Bhatt, and G. A. Lesieutre, "Adaptive piezoelectric energy harvesting circuit for wireless remote power supply," *IEEE Trans. Power Electron.*, vol. 17, no. 5, pp. 669–676, Sep. 2002.
[28] G. K. Ottman, H. F. Hofmann, and G. A. Lesieutre, "Optimized piezoelectric energy harvesting circuit using step-down converter in discontinuous conduction mode," *IEEE Trans. Power Electron.*, vol. 18, no. 2, pp. 696–703, Mar. 2003.
[29] E. Lefeuvre, D. Audigier, C. Richard, and D. Guyomar, "Buck-boost converter for sensorless power optimization of piezoelectric energy harvester," *IEEE Trans. Power Electron.*, vol. 22, no. 5, pp. 2018–2025, Sep. 2007.
[30] Z. J. Chew and M. Zhu, "Adaptive maximum power point finding using direct VOC/2 tracking method with microwatt power consumption for energy harvesting," *IEEE Trans. Power Electron.*, vol. 33, no. 9, pp. 8164–8173, Sep. 2018.
[31] C. Lu, C. Y. Tsui, and W. H. Ki, "Vibration energy scavenging system with maximum power tracking for micropower applications," *IEEE Trans. Very Large Scale Integration Syst.*, vol. 19, no. 11, pp. 2109–2119, Nov. 2011.
[32] Y. J. Hu, I. C. Chen, and T. H. Tsai, "A piezoelectric vibration energy harvesting system with improved power extraction capability," in *Proc. IEEE Asian Solid-State Circuits Conf.*, 2016, pp. 305–308.
[33] J. R. Liang and W. H. Liao, "Improved design and analysis of self-powered synchronized switch interface circuit for piezoelectric energy harvesting systems," *IEEE Trans. Ind. Electron.*, vol. 59, no. 4, pp. 1950–1960, Apr. 2012.

Ge Shi received the B.E. degree in electrical engineering and automation and the M.S. degree in detection technology and automation from China Jiliang University, Hangzhou, China, in 2004 and 2010, respectively, and the Ph.D. degree in micro-nano information system from Ningbo University, Ningbo, China, in 2018.

He is a Senior Experimentalist with China Jiliang University. His current research interests include energy harvesting systems, sensors and measuring technology, ultra-low power ICs design, and embedded system.

Yinshui Xia received the B.S. degree in physics and the M.S. degree in electronic engineering from Hangzhou University, Hangzhou, China, in 1984 and 1991, respectively, and the Ph.D. degree in electronic engineering from Edinburgh Napier University, Edinburgh, U.K., in 2003.

He was a Visiting Scholar with King's College London in 1999 and then joined Edinburgh Napier University as a Research Assistant and a Research Fellow from 2000 to 2005. He is currently a Professor with the Faculty of Electrical Engineering and Computer Science, Ningbo University, Ningbo, China. His research interests include low-power digital circuit design, logic synthesis and optimization, system on chip design, and energy harvesting systems.

Huakang Xia received the B.E. degree in aircraft design and engineering and the Ph.D. degree in instrument science and technology from Nanjing University of Aeronautics and Astronautics, Nanjing, China, in 2012 and 2017, respectively.

He is currently a Lecturer with the Faculty of Electrical Engineering and Computer Science, Ningbo University, Ningbo, China. His current research interests include energy harvesting system, ultra-low power circuit design, as well as embedded system.

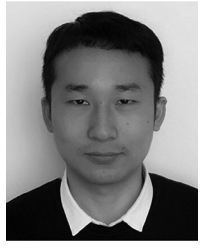

Xiudeng Wang was born in Xinyang, Henan, China, in 1992. He received the B.E. degree in communication engineering from Ningbo University, Ningbo, China, in 2016. He is currently working toward the M.S. degree with Ningbo University.

His research interests include energy harvesting systems, sensors and measuring technology, ultra-low power ICs design, as well as embedded system.

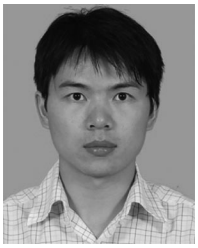

Libo Qian (M'15) received the B.E. degree in electron-mechanics, and the M.E. and Ph.D. degrees in microelectronics from Xidian University, Xi'an, China, in 2007, 2010, and 2013, respectively.

He currently serves as an Assistant Professor with the Faculty of Electrical Engineering and Computer Science, Ningbo University, Ningbo, China. His current research interests include 3-D ICs based on the through silicon vias and signal integrity of high-speed interconnect circuits.

Zhidong Chen received the B.E. degree in electronic and information engineering and the M.S. degree in electronic circuit and system from Hangzhou Dianzi University, Hangzhou, China, in 2011 and 2014, respectively. He is currently working toward the Ph.D. degree in Ningbo University, Ningbo, China.

He is currently a Lecturer with Zhejiang Business Technology Institute, Ningbo. His research interests include energy harvesting systems, and sensors and measuring technology.

Yidie Ye (M'18) received the B.E. degree in electronic engineering and the Ph.D. degree in circuits and systems from Zhejiang University, Hangzhou, China, in 2007 and 2012, respectively.

She is currently an Assistant Professor with the Faculty of Electrical Engineering and Computer Science, Ningbo University, Ningbo, China. Her current research interests include low-power circuit design and optimization.

Qing Li received the B.E. degree in industry electrical automation from the Harbin Institute of Technology, Harbin, China, in 1982.

He is currently a Professor with China Jiliang University, Hangzhou, China. His research interests include sensors and measuring technology.